Object-Orientated Filter Design in Spectral Domain for Polarimetric Weather Radar

Yin, Jiapeng; Unal, Christine; Russchenberg, Herman

DOI
10.1109/TGRS.2018.2876632

Publication date
2018

Document Version
Final published version

Published in
IEEE Transactions on Geoscience and Remote Sensing

Object-Orientated Filter Design in Spectral Domain for Polarimetric Weather Radar

Jiapeng Yin, *Student Member, IEEE*, Christine Unal, and Herman Russchenberg

***Abstract*— Aiming at removing stationary and moving clutter while retaining precipitation for dual-polarization weather radar, a new clutter suppression method, named the object-orientated spectral polarimetric (OBSpol) filter, is put forward in this paper. Based on the spectral polarimetric feature and the range-Doppler continuity of precipitation, the OBSpol filter generates a filtering mask implemented on the raw range-Doppler spectrogram to mitigate the clutter and noise. The procedures are as follows. After the spectral polarimetric filtering and the mathematical morphology method, one binary mask where "1" indicates the precipitation is obtained. Then, the contiguous bins of the same value "1" in the range-Doppler domain are grouped in areas termed as objects. Whether the produced objects are precipitation or not will be further judged based on appropriate weather radar observable. Thus, combining all the filtered separate objects, a filtering mask can be obtained. In this paper, data collected by the polarimetric Doppler IRCTR drizzle radar are used to demonstrate and assess the performance of the proposed technique in the case of ground clutter, narrowband moving clutter, and noise. Two precipitation cases are examined: 1) moderate precipitation with large scale and 2) light precipitation with severe clutter contamination. In the range-Doppler spectrogram, both stationary and narrowband moving clutters are mitigated, while maintaining nonoverlapping precipitation signal. This helps to solve the problem when clutter and precipitation overlap in the time domain. In addition, the OBSpol filter is proven to be effective with different Doppler velocity resolutions. This technique can be applied in real-time due to its low computation complexity. Moreover, the spectral polarimetric filtering can be designed using the measurements of dual-polarization radar systems which do not have cross-polar measurements. Hence, the proposed clutter mitigation technique can be implemented for operational dual-polarization weather radar.**

***Index Terms*— Dual-polarization weather radar, moving clutter, object-orientated, range-Doppler continuity, real-time clutter mitigation, spectral-polarimetry, weak precipitation signal.**

I. Introduction

WEATHER radar, sensing precipitation with high spatial and temporal resolution, is well recognized as an indispensable tool for atmospheric observation [1]. Upgrading to the polarimetric Doppler ability [2], weather radar can simultaneously record microphysical and dynamical features of precipitation, which largely improves its performance in quantitative precipitation estimation (QPE) [3], [4]. Weather radar data have also been used to forecast severe storms such as tornadoes and hurricanes [5]. In addition, the pluvial urban flood, which is caused by extreme rainfall and now a major societal hazard [6], can be predicted using radar measurements [7]. Not only is monitoring large-intensity precipitation important but also the weak precipitation such as drizzle. Accurate measurements of drizzle rates will improve our understanding of cloud lifetime, which is critical to climate change studies [8].

Generally, the prerequisite of using radar data for the QPE application is the sufficient measurement accuracy which is always affected by unwanted echoes, namely, radar clutter. However, compared with heavy precipitation, light precipitation may be easily removed by clutter mitigation methods. Hence, effective clutter suppression method should be developed to mitigate the clutter while keeping the precipitation regardless of its intensity.

Weather radar clutter mainly divides into two categories according to the Doppler velocity: stationary and nonstationary. One of the well-known stationary clutter (i.e., ground clutter) mitigation technique is named as the Gaussian model adaptive processing (GMAP) [9] which is introduced to resolve the problem when precipitation and ground clutter overlap. However, when GMAP is implemented on data without ground clutter contamination, it will result in some signal loss. Hence, ground clutter detection algorithms should be used before the application of GMAP. Integrating the clutter detection and filtering in one algorithm, the clutter environment analysis using adaptive processing (CLEAN-AP) is put forward [10]. Compared with GMAP, CLEAN-AP has a better clutter suppression performance, and the variance of estimates is diminished because of the usage of both magnitude and phase for proper notch width determination [11]. Nonetheless, GMAP and CLEAN-AP are not mitigation methods for moving clutter such as biomass and vehicles.

The nonstationary clutter for weather radar consists of flying biomass such as birds and insects, moving sea waves, variable radio frequency interference, and dynamic wind turbines. The feature studies of birds and insects are well documented in [12]–[15]. In addition, combining image processing techniques and the fuzzy logic algorithm, the sea and chaff clutter mitigation technique is proposed in [16]. The weather radar performance is significantly deteriorated by wind turbines because of the large-intensity backscattering from the

Manuscript received November 8, 2017; revised April 4, 2018, July 12, 2018, and September 20, 2018; accepted October 15, 2018. Date of publication November 5, 2018; date of current version April 22, 2019. The work of J. Yin was supported by the China Scholarship Council. *(Corresponding author: Jiapeng Yin.)*

The authors are with the Department of Geoscience and Remote Sensing, Faculty of Civil Engineering and Geoscience, Delft University of Technology, 2628 CN Delft, The Netherlands (e-mail: j.yin@tudelft.nl; c.m.h.unal@tudelft.nl; h.w.j.russchenberg@tudelft.nl).

Color versions of one or more of the figures in this paper are available online at http://ieeexplore.ieee.org.

Digital Object Identifier 10.1109/TGRS.2018.2876632

large tower and rotating blades [17], [18]. Techniques such as interpolation [19], [20], signal decomposition [21], and machine learning [22] are developed to remove the wind turbine clutter. Last but not least, the radio frequency interference arising from the radio local area network is also an annoying interference that brings the disturbances such as dots, spokes, and spikes in the radar plan position indicator (PPI) [23]. Similarly, artifacts caused by the radar system itself also affect the usage of radar data. Most of the time, the artifacts are speckles along many range bins in some azimuth directions in the PPI. Moreover, these speckles are nonstationary when observed in the Doppler domain, making it impossible to mitigate them with the conventional clutter suppression methods. These artifacts affect not only the reflectivity but also the Doppler and polarimetric measurements. For example, artifacts have influenced the polarimetric Doppler X-band radar IRCTR drizzle radar (IDRA) since its installation in 2007, which is well illustrated in [24] and [25]. Also, the high-resolution polarimetric Doppler X-band radar MESEWI suffers from this problem [26] and so do the Bonn X-band radar systems [27]. This specific type of moving clutter is studied in this paper.

A novel clutter suppression method named the object-orientated spectral polarimetric (OBSpol) filter is proposed to remove both stationary and nonstationary clutters while retaining as much precipitation as possible regardless of its intensity. Based on the spectral polarimetric feature and the range-Doppler continuity of precipitation, the OBSpol filter is implemented in the range-Doppler spectrogram (i.e., one ray in the radar PPI) to mitigate the clutter and noise. Generally, precipitation is continuous in the range-Doppler domain, and the OBSpol filter groups the contiguous bins into different independent objects after the spectral polarimetric filtering and the mathematical morphology method. Then, an extra observable is chosen to mitigate the clutter based on the separated objects. Since the ray-by-ray clutter mitigation technique is computationally efficient, it can be implemented in real time. In addition, the selected spectral polarimetric feature and extra observable can be a conventional variable of dual-polarization weather radar. Note that the term "conventional variable" refers to all variables available from a dual-polarization radar that does not have cross-polar measurements, including the standard moments (i.e., reflectivity, Doppler velocity, and spectral width) and the polarimetric observables (i.e., differential reflectivity, differential phase, and copolar correlation coefficient). Thus, the proposed clutter mitigation technique can be designed for dual-polarization operational weather radar.

Specifically, this paper will focus on the application of the OBSpol filter to IDRA narrowband clutter (both moving and stationary) mitigation and weak precipitation preservation. In this case, the extra observable will be the spectral width. The IDRA clutter can be also mitigated by a method named the moving double spectral linear depolarization ratio (MDsLDR) filter [24]. However, the MDsLDR filter requires measurements of a full-polarimetric weather radar. Hence, it is imperative to investigate one clutter mitigation method to remove the clutter and keep the weak precipitation for dual-polarization weather radar without cross-polar measurements. The OBSpol filter is put forward as an alternative for such a purpose. Similar spectral processing method, however not polarimetric, in mitigating ground clutter and narrowband interference for wind profiler radar is addressed in [28].

The structure of this paper is as follows. In Section II, the spectral polarimetric observables and the details of the proposed clutter suppression method are introduced. Then, using IDRA measurements, radar clutter analysis, filter parameter selection, and filter implementation are discussed in Section III. In Section IV, the OBSpol filter performance is compared with the MDsLDR filter and evaluated in the spectrogram and PPI. In addition, the effectiveness of the OBSpol filter with different Doppler velocity resolutions is explored. Finally, some conclusions are drawn in Section V.

II. Object-Orientated Spectral Polarimetric Filter

A. Spectral Polarimetric Observables

Based on the combined simultaneous Doppler and polarization information, spectral polarimetry exhibits the microphysical and dynamical properties of the target. This is favorable to retrieve the atmospheric microphysical information and to mitigate nonatmospheric echoes. Following the backscatter alignment convention, the spectral reflectivity which relates to the range r and Doppler velocity v is expressed as

$$sZ_{xy}(r,v) = C \cdot sP_{xy}(r,v) \cdot r^2 = C \cdot |S_{xy}(r,v)|^2 \cdot r^2 \quad (1)$$

where $S_{xy}(r,v)$ represents the complex Doppler velocity spectrum in range bin r with a transmitted y polarization and a receiving x polarization, x and y being horizontal polarization (i.e., h) or vertical polarization (i.e., v). In addition, $sP_{xy}(r,v)$ is defined as spectral power, and C is the calibration constant.

Accordingly, we can define the spectral differential reflectivity sZ_{dr}, the spectral linear depolarization ratio (sLDR) sLDR^{hh} and sLDR^{vv}, and the spectral copolar correlation coefficient $s\rho_{co}$ as

$$sZ_{dr}(r,v) = 10\log_{10}\left(\frac{sZ_{hh}(r,v)}{sZ_{vv}(r,v)}\right) \quad (2)$$

$$\text{sLDR}^{hh}(r,v) = 10\log_{10}\left(\frac{sZ_{vh}(r,v)}{sZ_{hh}(r,v)}\right)$$

$$\text{sLDR}^{vv}(r,v) = 10\log_{10}\left(\frac{sZ_{hv}(r,v)}{sZ_{vv}(r,v)}\right) \quad (3)$$

$$s\rho_{co}(r,v) = \frac{\left|\left\langle S_{hh}(r,v)S^*_{vv}(r,v)\right\rangle\right|}{\sqrt{\langle|S_{hh}(r,v)|^2\rangle\langle|S_{vv}(r,v)|^2\rangle}} \quad (4)$$

where $\langle\rangle$ represents the averaging which is calculated over a few neighboring range bins or Doppler bins. The latter is chosen in this paper, specifically a running average of seven consecutive Doppler bins for this paper. Note that there is no averaging for other observables except $s\rho_{co}$. The averaging makes the spectral polarimetric observables with lower variability, leading to thresholding technique working better in precipitation and clutter separation. However, the averaging will also broaden the clutter to its neighboring bins in the range-Doppler domain, resulting in incomplete clutter removal.

sZ_{dr} is a good indicator of the shape of hydrometeors, and it should be larger than 0 dB for oblate particles such as raindrops. It has also been investigated for clutter suppression in [29] to separate bird and insect echoes for wind retrievals. As for sLDR^{hh} and sLDR^{vv}, they are prone to contamination from clutter and noise, resulting in the increase of their values. Hence, sLDR can be used to distinguish the precipitation from clutter and noise. They have been used to mitigate clutter for an S-band atmospheric radar slant-wise or vertically profiling the troposphere [30]. The sLDR thresholding technique is enhanced for an X-band horizontally scanning radar [24]. However, most dual-polarization operational weather radar systems (e.g., WSR-88D [31], [32]) cannot measure the cross-polar backscattering. $s\rho_{co}$, which also proved to be an efficient classification observable [33], is available for most polarimetric radar systems. The spectral copolar correlation coefficient $s\rho_{co}$ is very close to 1 for most hydrometeors and significantly lower than 1 for nonmeteorological scatterers measured by the sidelobes of the antenna. However, for ground clutter, values of $s\rho_{co}$ are similar to that of precipitation while values of sLDR differ. This means that as a single spectral polarimetric parameter, sLDR is the most efficient in reducing different types of clutter [30]. To explore an effective clutter mitigation method for dual-polarization weather radar without cross-polar measurements, $s\rho_{co}$ is considered. However, to use $s\rho_{co}$ for both stationary and moving clutter mitigation, other techniques should be combined, which will be described in detail next.

After the spectral polarimetric filtering which is going to be proposed and discussed in this paper, only the bins representing the atmospheric signal are kept. Then, the standard moments and polarimetric observables can be calculated. The reflectivity in range bin r is expressed as

$$Z_{hh}(r) = C \cdot \sum_{v \in \text{atm}} (sP_{hh}(r, v) - sN) \cdot r^2 \tag{5}$$

where $v \in$ atm signifies that only those Doppler bins that contain atmospheric signal are used. sN is the spectral noise for the chosen spectrogram. By grouping all the power bins of sP_{hh} in a histogram, the power bin related to the largest number frequency will be regarded as the estimated spectral noise. The spectrogram-by-spectrogram noise estimation is inspired in [34], which is proposed to accurately produce estimates of the system noise power. In addition, the radial velocity $\bar{v}$ and spectral width σ_v can be expressed as

$$\bar{v}(r) = \frac{1}{Z_{hh}(r)} \sum_{v \in \text{atm}} v \cdot sZ_{hh}(r, v) \tag{6}$$

$$\sigma_v(r) = \sqrt{\frac{1}{Z_{hh}(r)} \sum_{v \in \text{atm}} (v - \bar{v}(r))^2 \cdot sZ_{hh}(r, v)}. \tag{7}$$

Finally, the copolar correlation coefficient is defined as

$$\rho_{co}(r) = \frac{\left|\sum_{v \in \text{atm}} \left\langle S_{hh}(r, v) S^*_{vv}(r, v) \right\rangle\right|}{\sqrt{\sum_{v \in \text{atm}} \langle |S_{hh}(r, v)|^2 \rangle \sum_{v \in \text{atm}} \langle |S_{vv}(r, v)|^2 \rangle}}. \tag{8}$$

These four radar observables will be evaluated after the application of the proposed filter in Section IV.

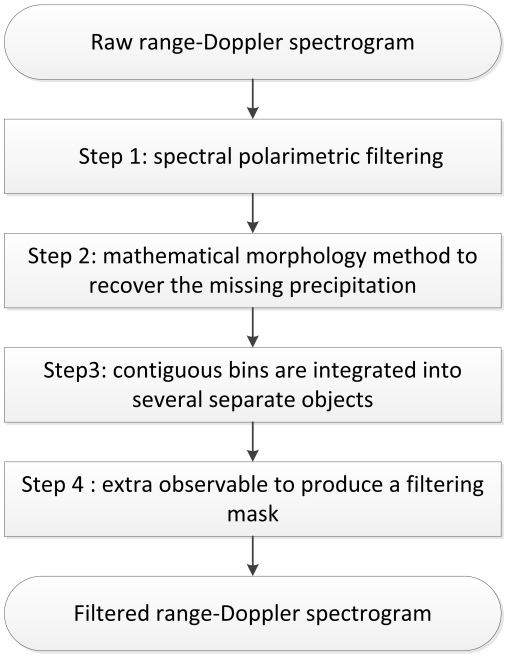

Fig. 1. Flowchart of the OBSpol filter.

B. Filter Description

Taking advantage of the spectral-polarimetric feature and the range-Doppler continuity of precipitation, the OBSpol filter is implemented in the range-Doppler spectrogram. This clutter mitigation technique contains four steps, and its flowchart is shown in Fig. 1. The input of the OBSpol filter is the raw range-Doppler spectrogram while the output will be the filtered one. The raw range-Doppler spectrogram is obtained by applying the Fourier transform along the sample time with a Hamming window.

Step 1: One precipitation mask is obtained by the spectral polarimetric filtering.

1) sLDR Is Not Available: For dual-polarization radar systems without cross-polar measurements, the spectral copolar correlation coefficient $s\rho_{co}$ is always available. Filtered by the $s\rho_{co}$, the binary mask $M^{s\rho_{co}} \in \{0, 1\}$ indicating precipitation is expressed as

$$M^{s\rho_{co}} = \begin{cases} 1, & if\ s\rho_{co} > T_1 \\ 0, & \text{otherwise} \end{cases} \tag{9}$$

where the threshold T_1 can be set based on the clutter and precipitation removal percentage. Since ground clutter and precipitation have a similar $s\rho_{co}$ value distribution, $M^{s\rho_{co}}$ will keep ground clutter, which means that another ground clutter mitigation method should be added. The narrow notch filter around 0 ms^{-1} or even more advanced techniques such as GMAP and CLEAN-AP can be used to remove the ground clutter. With such implementation, a ground clutter mitigation mask $M^{\text{GCM}} \in \{0, 1\}$ where "0" indicates that ground clutter will be developed. Note that the spectral copolar correlation coefficient filtering is implemented on the whole spectrogram while the ground clutter mitigation

is only concentrated around 0 ms^{-1}, and the remaining bins will be set to "1" in M^{GCM}. Then, after the completion of Step 1, one binary mask $M^{\text{step1}} \in \{0, 1\}$ can be obtained, expressed as

$$M^{\text{step1}} = M^{s\rho_{co}} \times M^{\text{GCM}}. \tag{10}$$

2) sLDR Is Available: For radar systems with full-polarimetric measurement capability, the sLDR can be used to mitigate the clutter, moving and stationary. Then, the binary filtering mask in Step 1 can be directly obtained and expressed as

$$M^{\text{step1}} = \begin{cases} 1, & \text{if } \text{sLDR}^{hh} < T_2, \quad \text{sLDR}^{vv} < T_2 \\ 0, & \text{otherwise} \end{cases} \tag{11}$$

where the threshold T_2 is set based on clutter and precipitation removal percentage.

The precipitation mask M^{step1} is obtained based on the spectral polarimetric features of precipitation and clutter, which may cause some precipitation loss due to the low signal-to-noise ratio (SNR). When the SNR is low, the spectral polarimetric values of precipitation and clutter tend to overlap. Using a fixed thresholding method in Step 1, it may remove weak precipitation. The relation between spectral polarimetric observable value distributions and SNR will be given later combined with radar measurements. In addition, some noise will be kept, which will be removed in the following steps.

Step 2: The mathematical morphology method is used to recover the missing precipitation.

The mathematical morphology which is widely used in the binary image analysis can be used to recover the missing precipitation. The basic morphological operators contain erosion, dilation, opening, and closing [35], and specifically closing is selected here. Closing is defined as the combination of dilation followed by erosion. Dilation operator with proper structuring element fills the holes inside M^{step1}, but extends the perimeter of the range-Doppler areas with value "1," which can be restored by performing the erosion operator with the same structuring element. A structuring element is a shape, used to probe or interact with a given image, with the purpose of drawing conclusions on how this shape fits or misses the shapes in the image. In this paper, the structuring element is selected as a flat disk of radius r, because precipitation is continuous in the range-Doppler spectrogram and flat disk is better in smoothing the precipitation boundaries. The selection of radius r will be discussed in a systematic way in Section III. After the completion of Step 2, one binary mask $M^{step2} \in \{0, 1\}$ is obtained.

Step 3: The contiguous bins having value "1" are integrated into several separate objects.

Taking advantage of the range-Doppler continuity of precipitation, the contiguous bins of the same values "1" are grouped in areas in the range-Doppler domain which are termed as objects. These bins are termed as connected bins. The basic steps in finding the connected bins are shown in Table I [36].

TABLE I
CONNECTED RANGE-DOPPLER BINS LABELING ALGORITHM

i) Search for the next unlabeled bin p having value "1"
ii) Use a flood-fill algorithm [37] to label bin p
iii) Repeat steps i) and ii) until all the bins are labeled.

Note that the unlabeled bin is a bin not yet attributed to one object. The flood-fill algorithm is universally used in the field of image processing to determine the areas connected to a given bin (i.e., a pixel). In the situation of the binary mask generation, the neighboring bins indicating "1" of an unlabeled bin "1" will be integrated together into one object. Depending on whether we consider contiguous bins touching at the corners connected or not, two options—eight neighbors and four neighbors—can be considered. Since precipitation is continuous in the range-Doppler domain, eight neighbors option is selected here. After objects are separated, they are sorted in area descending order going from the largest area to the smallest one, as $\mathbf{O} = [O_1, O_2, \ldots, O_N]$. Normally, precipitation is continuous in the range-Doppler spectrogram, and it has two properties: 1) large area sizes and 2) limited numbers of objects. Hence, only a limited number of separated objects that exhibit the largest areas in $\mathbf{O}$ will be chosen for processing in Step 4.

Step 4: Extra observable is used to produce the filtering mask.

The sorted objects in $\mathbf{O}$ will be taken one by one and further classified as precipitation or not. Inspired by the better performance of the object-orientated technique in remote sensing data analysis than the pixel-based technique [38], we propose similar object-orientated precipitation and clutter separation technique. In addition to spectral polarimetric observable values, other information, such as shape, can be also used in the new filter design. Therefore, it can take full advantage of the range-Doppler continuity property of precipitation in the filter design. If the selected objects in $\mathbf{O}$ contain both precipitation and clutter, it means that they have similar spectral polarimetric observable values and area sizes. Thus, separation should be performed with extra observables to further remove the clutter. Which observables should be combined to complete the precipitation and clutter separation depends on the type of clutter and its property. For a given $O_i \in \mathbf{O}$, the filtered mask is expressed as M_{O_i}. After the extra observable filtering, the filtered separate objects are integrated as one mask expressed as

$$M^{\text{step4}} = \sum_{i=1}^{N} M_{O_i}. \tag{12}$$

$M^{\text{step4}} \in \{0, 1\}$ is the final mask applied to the raw range-Doppler spectrogram to remove the clutter and noise and preserve the precipitation. One scenario will be studied in detail using radar data in Section III.

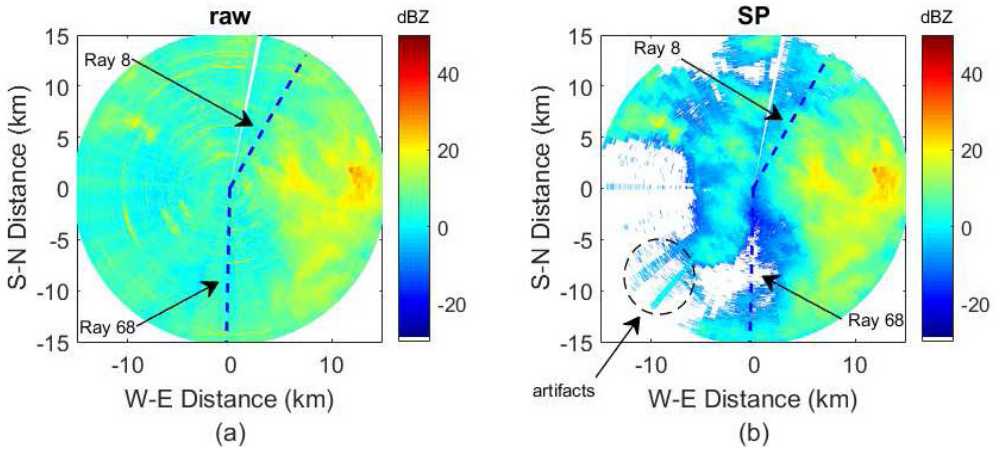

Fig. 2. Reflectivity PPI of IDRA. Data measured at 13:00 UTC on August 22, 2014. (a) Raw Z_{hh}. (b) Z_{hh} after standard processing.

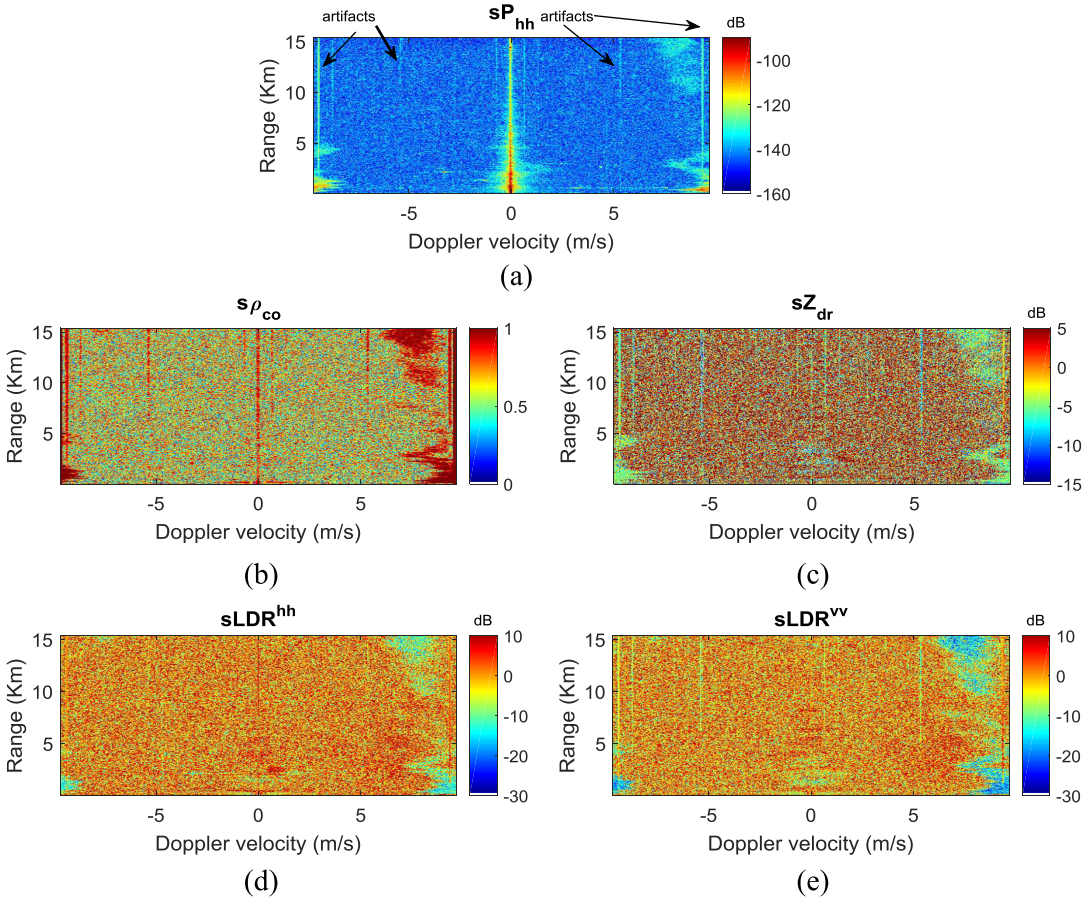

Fig. 3. Spectral polarimetric observables of IDRA. Data are related to Ray 68 of the measurements at 13:00 UTC on August 22, 2014. (a) Spectral power sP_{hh}. (b) Spectral copolar correlation coefficient $s\rho_{co}$. (c) Spectral differential reflectivity sZ_{dr}. (d) sLDR^{hh}. (e) sLDR^{vv}.

III. Application to Radar Data

A. Radar Clutter Analysis

The X-band polarimetric Doppler IDRA observes continuously the atmosphere [39], and it updates its measurements shown in near real-time online [40] with a rotation rate 1 rpm. All the data collected by this horizontally scanning radar from April 2009 up to now can be accessed on the website named 4TU.center for Research Data [41]. However, IDRA has been affected by narrowband moving clutter (also termed as artifacts) since its installation in 2007, which is well documented in [24] and [25]. The specifications of the linear frequency-modulated continuous waveform (FMCW) radar are shown in Table II. Note that the number of sweeps, which is the terminology for FMCW radar, is equivalent to the number of pulses for pulse radar.

The raw PPI of one radar measurement at 13:00 UTC on August 22, 2014 is shown in Fig. 2(a). In addition, the PPI after the standard clutter suppression processing is shown in Fig. 2(b) for a comparison. The standard processing is carried out in the range-Doppler domain. It consists of a narrow notch filter centered around 0 ms^{-1} and the double

TABLE II
IDRA SPECIFICATIONS [39]. BOLDFACE: PARAMETERS USED FOR THE OPERATIONAL MODE

Radar type	Linear FMCW
Polarization	Full polarimetric
Center frequency (GHz)	9.475
Transmitted power (W)	1, 2, 5, 10, **20**
Range resolution (m)	3, 6, 15, **30**
Sweep time (μs)	204.8, **409.6**, 8192.2, 1638.4, 3276.8
Frequency sweep (MHz)	**5**, 10, 20, 50
Antenna beamwidth (○)	1.8
Elevation angle (○)	0.5

sLDR filter [30]. Furthermore, a spectral noise clipping technique is implemented. It keeps the Doppler bins related to a spectral power at least 3 dB above the spectral noise level. Finally, Doppler spectra containing less than 2% of valid Doppler bins are discarded. From Fig. 2(b), the remaining artifacts are indicated in some azimuths. It means that the standard processing is ineffective at artifact removal. Actually, the azimuths displaying artifacts are not fixed among different PPIs from the long-term observation.

To take a closer look at the raw range-Doppler spectrogram (i.e., one ray in radar PPI), Ray 68 is extracted and the spectral polarimetric observables are shown in Fig. 3. Recall that in Section II-A, averaging is not carried out to obtain sP_{hh}, sZ_{dr}, sLDR^{hh}, and sLDR^{vv}; however, a running average of seven consecutive Doppler bins is used for $s\rho_{co}$. The properties of artifacts can be observed as follows: 1) nonstationary in the Doppler domain; 2) randomly appearing in some range bins; 3) parts of its intensity larger than that of weak precipitation; and 4) similar spectral polarimetric features with precipitation. These features make it difficult to suppress this specific clutter for weather radar. Furthermore, Range bin 468 (e.g., 14 km) is taken and its power spectrum, $s\rho_{co}$ spectrum and sLDR^{vv} spectrum are plotted as shown in Fig. 4. As is observed, the power intensity of ground clutter and some artifacts is higher than that of precipitation. After integrating the whole Doppler bins resulting in one reflectivity value, the true reflectivity of precipitation will be biased by the artifacts and ground clutter. Fortunately, the spectral width of artifacts and ground clutter is much narrower compared with that of precipitation, which can be used as the extra observable in Step 4 for the OBSpol filter design. Moreover, $s\rho_{co}$ values of precipitation and clutter are inseparable, which is different from that of noise. When $s\rho_{co}$ is chosen, another technique should be combined to mitigate the ground clutter. While precipitation has different sLDR^{vv} values from that of clutter and noise, indicating sLDR as a powerful clutter and precipitation separation observable.

As is mentioned in Section I, the MDsLDR filter is put forward to remove the narrowband clutter (i.e., radar artifacts and ground clutter) for full-polarimetric weather radar. Based on the difference of the spectral polarimetric feature and the spectral continuity between precipitation and clutter, the method is proven to be effective and its performance is verified by data collected in different scenarios. However, the limitation of applying the MDsLDR filter in dual-polarization weather radar which does not measure cross-polar backscattering is

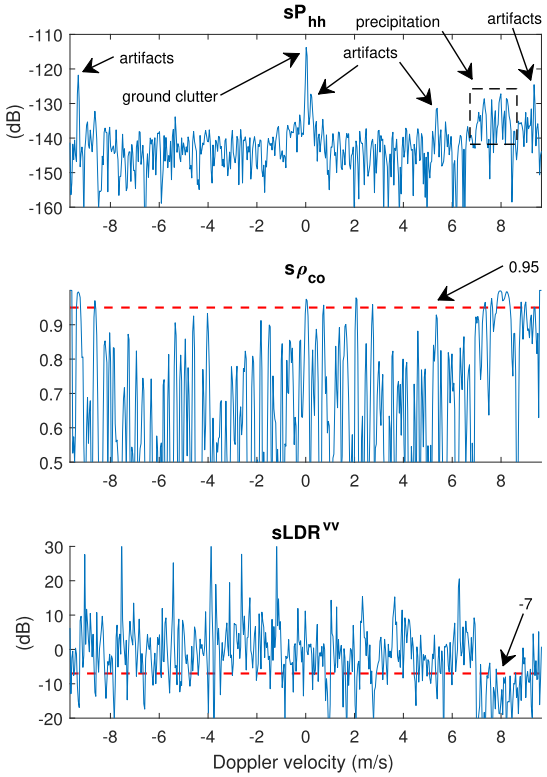

Fig. 4. Observable spectra of Range bin 468 (e.g., 14 km). (a) Spectral power sP_{hh}. (b) Spectral copolar correlation coefficient $s\rho_{co}$. (c) sLDR^{vv}.

the sLDR measurements. The OBSpol filter proposed in this paper is used to fill the gap and the performance of the two filters will be compared and discussed in detail next.

B. Parameter Selection

Retaining the precipitation and removing the clutter is always a tradeoff. In Step 1 of the OBSpol filter, for dual-polarization weather radar without cross-polar measurements, the spectral copolar correlation coefficient $s\rho_{co}$ is used as the spectral polarimetric observable for nonmeteorological scatterer mitigation. Furthermore, the notch filter around 0 ms^{-1} is used to generate the ground clutter mitigation mask M^{GCM}. Note that Doppler velocities between -0.23 and 0.23 ms^{-1} (i.e., 13 Doppler bins for IDRA operational mode with 512 sweeps for Doppler processing) are used to generate the M^{GCM}, which is based on the statistical analysis of spectral width of ground clutter. The selection of the thresholds T_1 and T_2 is based on the precipitation and clutter removal percentage [24], [30], specifically $T_1 = 0.95$ and $T_2 = -7$ dB.

Considering Ray 8 and Ray 68 of raw PPI in Fig. 2(a), the true precipitation areas are manually selected in the range-Doppler spectrogram, and the $s\rho_{co}$ and sLDR (i.e., sLDR^{hh} and sLDR^{vv}) value distributions versus SNR are calculated, as shown in Fig. 5. Note that since the filter design is implemented in the spectral domain, SNR is defined as

$$\text{SNR}(r) = \frac{\sum_v (sP_{hh}(r, v) - sN)}{\sum_v sN}. \tag{13}$$

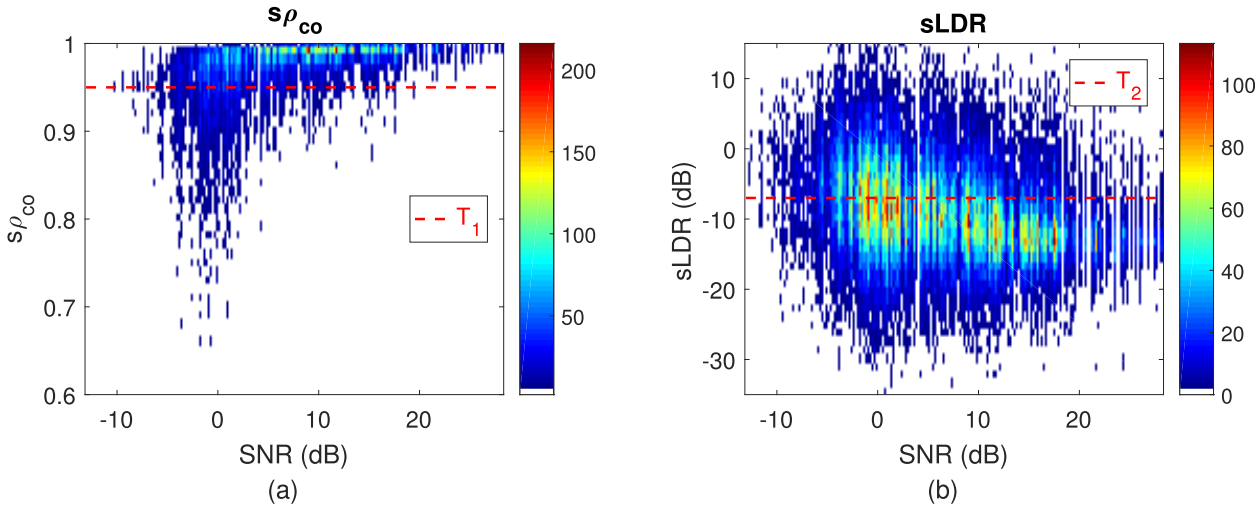

Fig. 5. Spectral polarimetric observable distributions of precipitation versus SNR. (a) $s\rho_{co}$. (b) sLDR^{hh} and sLDR^{vv}.

Therefore, for each range bin, we can calculate one SNR and it corresponds to several spectral polarimetric observable values. The estimation of noise is based on the noise measurements by the radar system. From Fig. 5(a) and (b), it is concluded that both $s\rho_{co}$ and sLDR have larger distributions with the decrease of SNR. This means that using $s\rho_{co}$ and sLDR as the spectral polarimetric filtering observables in weather radar may cause some weak precipitation loss. Hence, other techniques should be included to preserve weak precipitation. In this paper, we aim to propose one technique for dual-polarization weather radar which does not measure cross-polar backscattering, so the focus is on the combination of the $s\rho_{co}$ filtering and notch filter around 0 ms^{-1}.

For the parameter selection next, Ray 68 of raw PPI in Fig. 3(a) is chosen as the study case. In Step 2, the structuring element is chosen as the flat disk of radius r which will be discussed here. First, we define P_d as the detection probability of precipitation which is the ratio between the precipitation areas after Step 2 and the true precipitation areas

$$P_d = \frac{N_s}{N_s + N_f} \tag{14}$$

where N_s is the number of precipitation bins successfully identified and N_f is the number of precipitation bins classified as clutter and noise. The false alarm rate (detecting the clutter and noise) P_{fa} is defined as the clutter and noise areas after Step 2 divided by the true nonprecipitation ones

$$P_{fa} = \frac{N_i}{N_T - N_s - N_f} \tag{15}$$

where N_T is the total bin number of the chosen spectrogram, and N_i is the number of clutter and noise bins classified as precipitation. The relations between the calculated P_d and P_{fa} and different structuring element size r are shown in Fig. 6. Normally, with the increase of radius r, both P_d and P_{fa} will increase, which is consistent in this figure. On the one hand, when the radius r is in the interval of [1, 3], P_d increases rapidly while P_{fa} increases slowly. On the other hand, when r is in the interval of [3, 7], the situation is opposite. Thus,

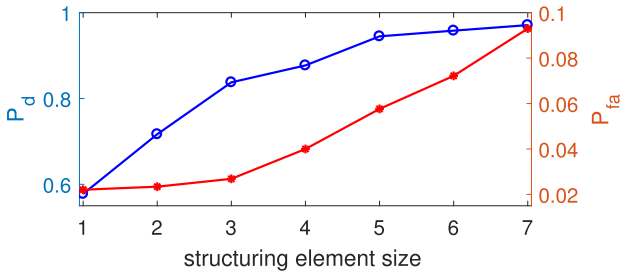

Fig. 6. Structuring element size versus P_d and P_{fa}.

$r = 3$ is the turning point where the detection probability of precipitation is sufficient while keeping low false alarm rate. Based on this analysis, the structuring element size r is chosen to be 3.

Finally, in Step 4, the extra observable selected for IDRA precipitation and artifact separation is the spectral width. In general, precipitation is the distributed target with large spectral width. On the contrary, artifacts are narrowband moving clutter with limited spectral width, specifically the largest Doppler spectral width L observed equals five Doppler bins (about 20 cms^{-1}) for IDRA in the operational mode. Considering the mathematical morphology adopted in Step 2, the threshold T_3 for the spectral width selection will be

$$T_3 = L + 2 \times r \tag{16}$$

where r is the structuring element size determined in Step 2. Hence, we have $T_3 = 11$ (about 42 cms^{-1}). It means that for the separated objects obtained in Step 3, those range bins related to one object whose spectral width is less than T_3 will be discarded. Therefore, dealiasing of the Doppler spectra should be carried out before this filtering technique to avoid the presence of narrowband precipitation Doppler spectra due to Doppler aliasing. Note that the calculation of the filtered spectral width in each range bin is by summing up the binary separated objects along the Doppler domain.

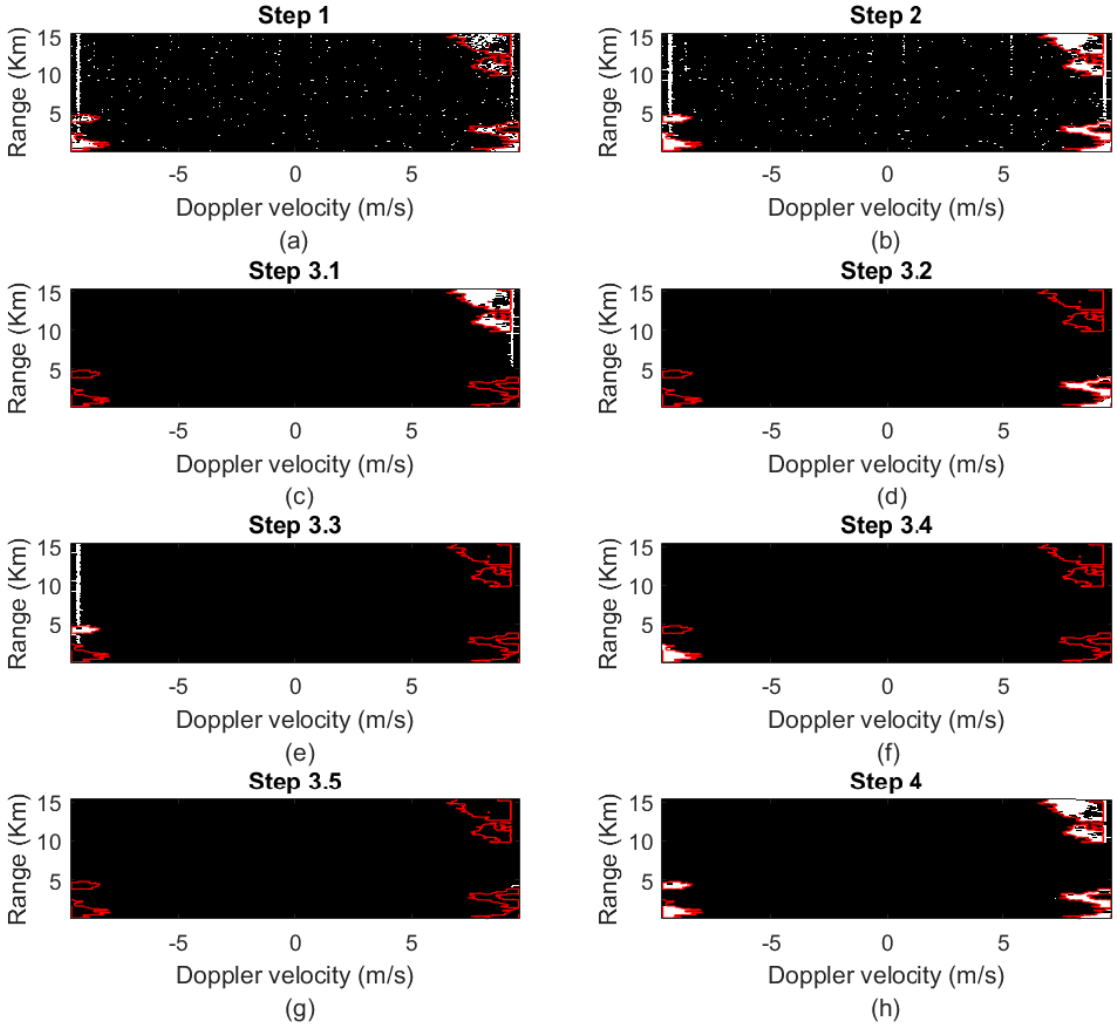

Fig. 7. Output range-Doppler masks after each step of the flowchart. (a) Step 1. (b) Step 2. (c)–(g) Step 3. (h) Step 4.

The above-mentioned analysis provides the parameter selection for the OBSpol filter applying to the IDRA data in the case of narrowband clutter (both moving and stationary).

C. Implementation

With the set of the selected parameters, the implementation of the OBSpol filter will be given step by step according to the flowchart in Fig. 1. The results are the binary spectrograms, as shown in Fig. 7 where white color represents precipitation and the red contour represents the true precipitation obtained by manual selection. First, in Step 1, the $s\rho_{co}$ filtering and the notch filter around 0 ms^{-1} are combined to generate the binary filtering mask. From Fig. 7(a), the range-Doppler mask after the spectral polarimetric filtering is not sufficient because of the remaining artifacts and noise. In addition, there are some missing points inside the precipitation areas. Second, with the mathematical morphology in Step 2, Fig. 7(b) shows the recovery of the missing precipitation, but also an increase in artifacts and noise. Third, the connected range-Doppler bins are integrated into several separate objects as shown in Fig. 7(c)–(g), where their subtitles represent the descending orders in areas, namely, from the largest area to the smallest one. As is mentioned in Section II, a limited number of separated objects that exhibit the largest areas will be chosen for the next process, and here, only the top five are shown because only the fifth one [i.e., Fig. 7(g)] contains some isolated noise. The number of separate objects chosen for next step should not be too small; otherwise, it will cause precipitation loss. Neither should it be too large, otherwise it will keep extra artifacts or noise, which is not a problem because they can be removed by the extra observable filtering in Step 4 (i.e., the spectral width). For the empirical setting, we select the top eight objects for next step processing. Note that Fig. 7(c) and (e) show the situations where precipitation and artifacts overlap. Finally, with the spectral width filtering, and integrating all the filtered areas in one mask as indicated by (12), we obtain Fig. 7(h) as the filtering mask on the raw range-Doppler spectrogram. There is some signal loss around 4 km, and this originates from the Doppler aliasing which separates one precipitation area into two parts. It is expected that the signal loss problem can be avoided with proper dealiasing technique [42] which will integrate the separated precipitation as a whole and increase the spectral width. Note that the OBSpol filter cannot resolve the situation when precipitation and clutter overlap.

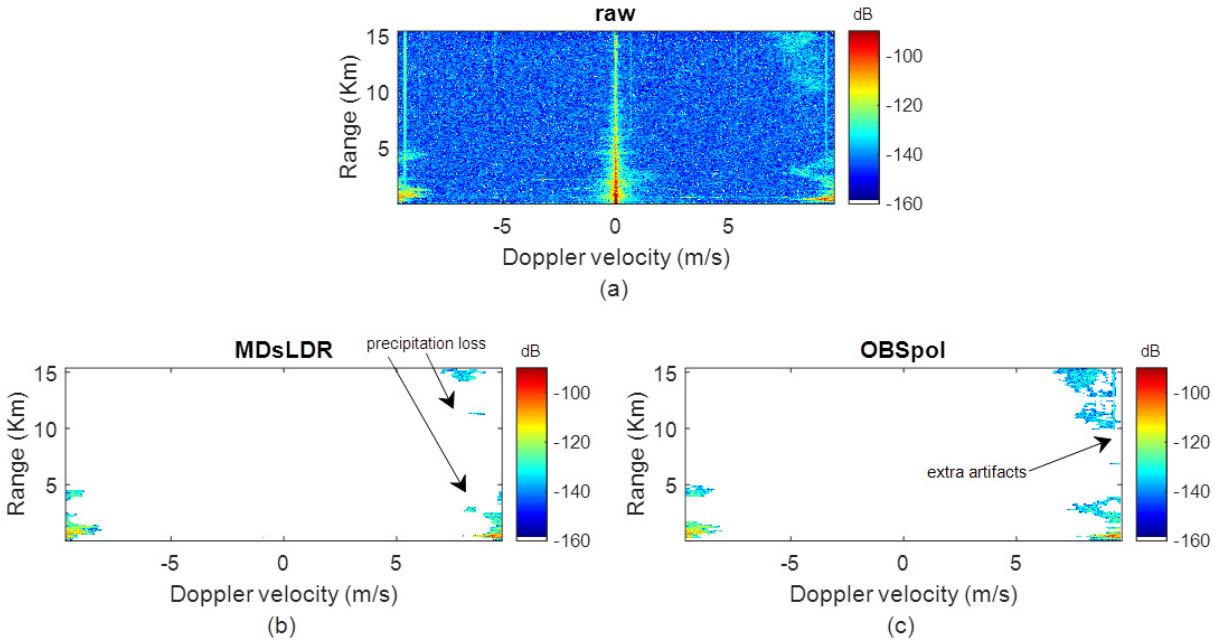

Fig. 8. Qualitative performance comparison between MDsLDR and OBSpol filters. (a) Raw sP_{hh} spectrogram. (b) MDsLDR-filtered sP_{hh} spectrogram. (c) OBSpol-filtered sP_{hh} spectrogram.

IV. Filter Performance Evaluation

A. Spectrogram Analysis

In this section, the performance of the OBSpol filter applied to IDRA measurements will be further discussed qualitatively and quantitatively comparing with one existing filter named the MDsLDR filter. The results of the MDsLDR filter and the OBSpol filter implemented on the raw range-Doppler spectrogram sP_{hh} in Fig. 3(a) are shown in Fig. 8. Note that raw spectrogram sP_{hh} means spectrogram without any processing. From Fig. 8(b) and (c), it is clear that both filters can remove the artifacts, ground clutter, and noise, while the OBSpol filter outperforms in keeping more weak signal. However, it retains some artifacts that overlap with precipitation.

To quantify the filter performance, the SNR is calculated and shown in Fig. 9(a). It can be concluded that both MDsLDR filter and OBSpol filter can retain the precipitation when the SNR is larger than 2 dB. When the SNR is smaller than 2 dB, sometimes, there is some signal missing in the MDsLDR filter and there is no such problem with the OBSpol filter [see the black arrows "signal loss" in Fig. 9(a)]. Furthermore, the power difference between the filtered one and the true one is obtained in Fig. 9(b). Note that the true power is obtained by the manual selection of precipitation in the raw range-Doppler spectrogram. The maximum power difference for the OBSpol filter is around 5 dB while that of the MDsLDR filter is 10 dB. Note that such conclusion is given based on the premise that the true SNR is smaller than 0 dB which usually corresponds to light precipitation or drizzle.

Finally, the root-mean-square error (RMSE) is used to quantify the filtering performance. Supposing a given spectrogram, where we have R range bins with precipitation, the RMSE of a specific observable X can be expressed as

$$\delta X = \sqrt{\frac{1}{R}\sum_{r=1}^{R}(X^{\mathrm{tru}}(r) - X^{\mathrm{est}}(r))^2} \tag{17}$$

where $X^{\mathrm{tru}}(r)$ is the true observable value in the rth range bin, which is manually selected, and $X^{\mathrm{est}}(r)$ is the filtered observable value in the rth range bin. Note that the observable X can be reflectivity Z_{hh}, radial velocity $\bar{v}$, spectral width σ_v, and copolar correlation coefficient ρ_{co}. The δZ_{hh} and $\delta\rho_{co}$ of the MDsLDR filter are 2.58 dBZ and 0.063 while that of the OBSpol filter are 2.06 dBZ and 0.100 for this spectrogram (i.e., Ray 68). The RMSE difference is due to the precipitation loss in the MDsLDR filter and the artifacts preservation in the OBSpol filter, both of which are labeled in Fig. 8. The RMSE of the $\bar{v}$ and σ_v are not provided because the chosen spectrogram is Doppler aliased which will bring in bias. Note that the SNR interval of the chosen spectrogram is [−15 dB, 23 dB] which includes weak and moderate precipitation. To quantify further these observables, we use another data (measured at 02:00 UTC on July 01, 2011) which do not have the problem of Doppler aliasing. Continuous rays from Ray 45 to Ray 54 are considered and the true values are manually selected. These rays are selected because clutter and precipitation do not overlap in order to estimate properly the true values of precipitation. The results are shown in Table III. In addition, the SNR histogram of the chosen data is displayed in Fig. 10. Distributed in the interval of [−15 dB, 43 dB], the selected data contain weak, moderate, and strong precipitation. In general, both the OBSpol filter and the MDsLDR filter have good performance, specifically the average δZ_{hh} is within 1.00 dBZ, the average $\delta\bar{v}$ within 0.15 m/s, the average $\delta\sigma_v$ within 0.50 m/s and the average $\delta\rho_{co}$ within 0.020.

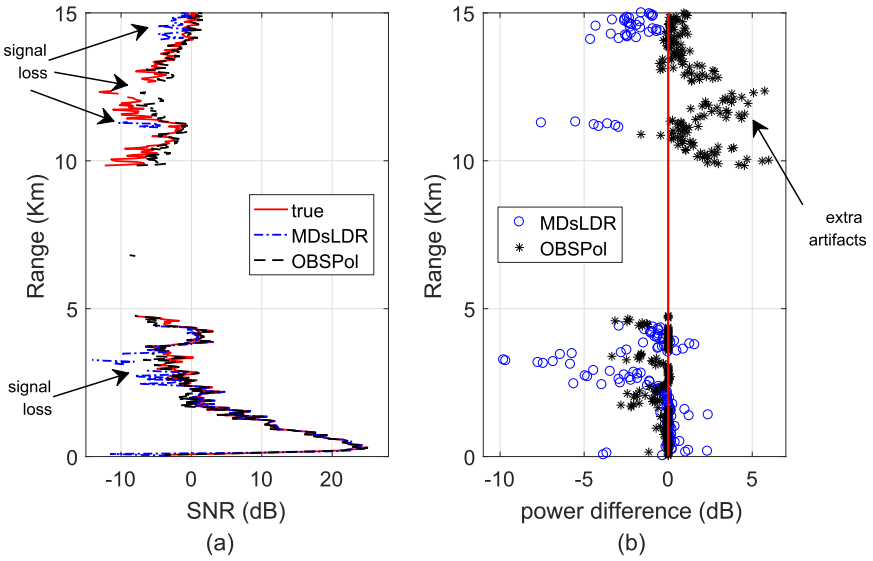

Fig. 9. Quantitative performance comparison between MDsLDR and OBSpol filters. (a) SNR calculation in different range bins. (b) Power difference after MDsLDR and OBSpol filters.

TABLE III
RMSE OF RADAR OBSERVABLES

Ray No.	MDsLDR				OBSpol			
	δZ_{hh}	$\delta\bar{v}$	$\delta\sigma_v$	$\delta\rho_{co}$	δZ_{hh}	$\delta\bar{v}$	$\delta\sigma_v$	$\delta\rho_{co}$
45	1.60	0.05	0.07	0.017	0.49	0.06	0.05	0.013
46	1.05	0.75	0.82	0.037	0.43	0.55	0.74	0.023
47	0.83	0.05	0.09	0.003	0.19	0.01	0.08	0.002
48	1.43	0.13	0.20	0.012	0.05	0.02	0.03	0.003
49	1.57	0.15	0.16	0.018	0.08	0.02	0.02	0.005
50	0.17	0.04	0.14	0.002	0.03	0.06	0.21	0.002
51	1.30	0.05	0.07	0.061	0.59	0.02	0.03	0.015
52	0.29	0.04	0.04	0.005	0.24	0.02	0.02	0.011
53	0.63	0.07	0.04	0.005	0.05	0.02	0.02	0.004
54	0.93	0.15	0.49	0.010	0.57	0.11	0.42	0.019
average	1.00	0.15	0.45	0.017	0.27	0.09	0.16	0.010

The OBSpol filter outperforms the MDsLDR filter in all the observables when clutter and precipitation do not overlap and Doppler dealiasing had been performed. It means that the OBSpol filter has a better performance in weak precipitation preservation.

B. PPI Analysis

For operational weather radar systems, the filtered observables are required to display in real time in the radar PPI. To test the real-time capability of the proposed technique, both the MDsLDR and OBSpol filters are applied to the data collected at 13:00 UTC on August 22, 2014 and their results are given in Fig. 11. Compared with the PPI after the standard processing shown in Fig. 2(b), both the MDsLDR filter [i.e., Fig. 11(a)] and the OBSpol filter [i.e., Fig. 11(b)] have better performance in artifact removal, while the OBSpol-filtered PPI performs better in weak precipitation preservation. One example is the Ray 68 (i.e., Fig. 8) which corresponds to the spectrogram analyzed mentioned above. It is not easy to obtain the true precipitation for the selected data, and the ray-by-ray output check is done to further verify the better performance of the OBSpol filter in keeping weak precipitation signal. All the following cases are met: precipitation with narrowband clutter and precipitation with ground clutter. Note that the implementation of the MDsLDR and OBSpol filters takes 18.2 and 28.1 s for the whole PPI using MATLAB 2016b in a Window 7 desktop PC with a 3.6-GHz Intel Xeon E5-1620 CPU and 16-GB RAM in this case. Hence, both algorithms can be implemented in real time.

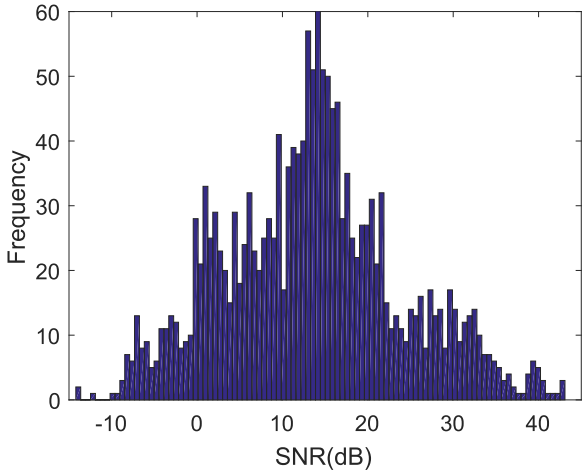

Fig. 10. SNR histogram of the chosen data for RMSE evaluation.

To further quantify the filtering performance of the OBSpol filter in the PPI, the clutter suppression ratio (CSR) is calculated and plotted in Fig. 11(c). In principle, CSR is the filtered reflectivity subtracted from the raw one. The maximum CSR is 54.7 dB for the case occurred at 13:00 UTC on August 22, 2014. Furthermore, the scatter plot of the MDsLDR-filtered reflectivity Z_{hh}^{MDsLDR} and the OBSpol-filtered reflectivity Z_{hh}^{OBSpol} is shown in Fig. 11(d). Most of the time, when the reflectivity is less than 10 dBZ, Z_{hh}^{OBSpol} is larger than Z_{hh}^{MDsLDR}. This is because the OBSpol filter has better ability in retaining weak precipitation. As for the unexpected cases where Z_{hh}^{OBSpol} is smaller than Z_{hh}^{MDsLDR},

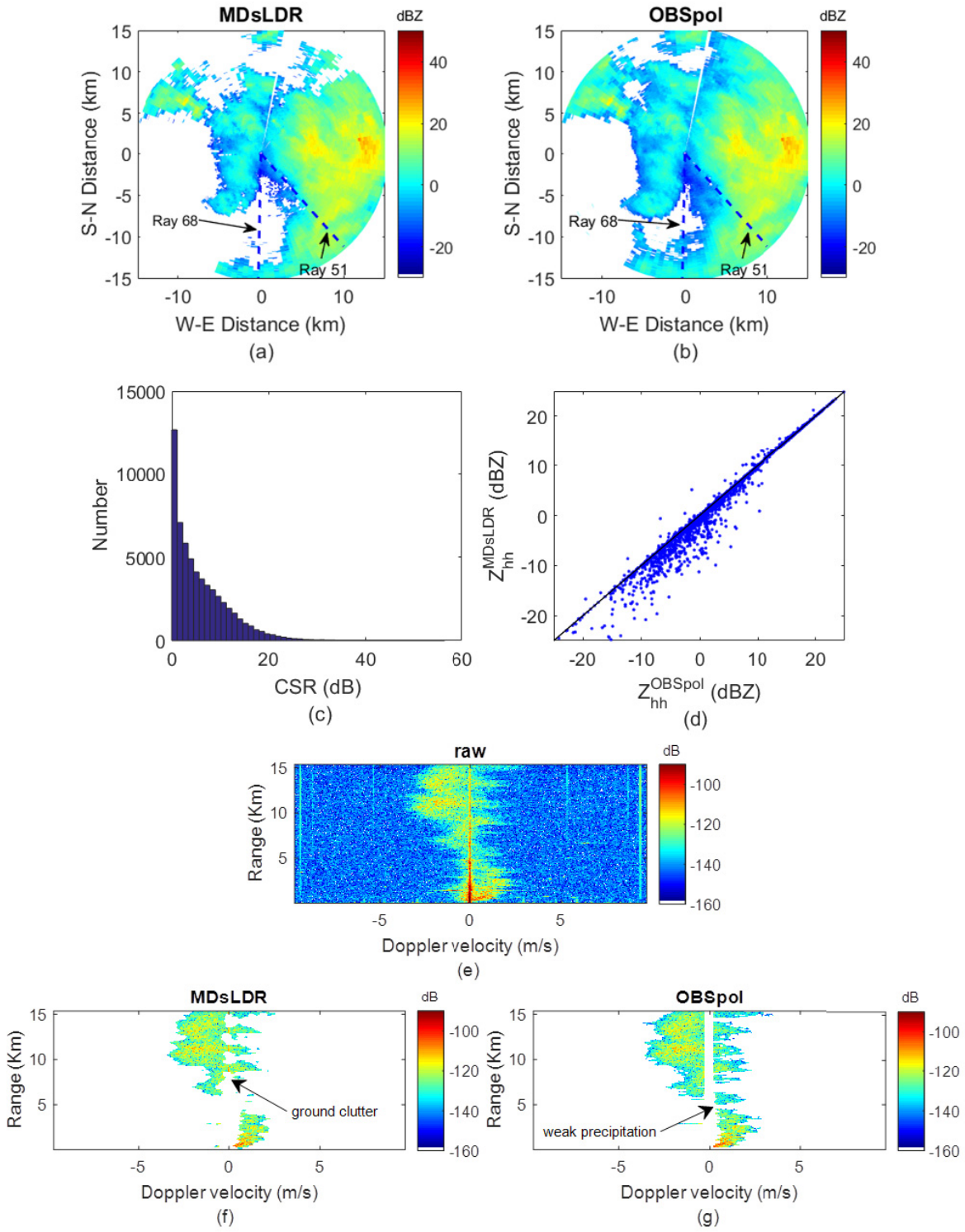

Fig. 11. Performance comparison between MDsLDR and OBSpol filters. Data measured at 13:00 UTC on August 22, 2014. (a) Z_{hh} after the MDsLDR filter. (b) Z_{hh} after the OBSpol filter. (c) CSR distribution of the OBSpol filter. (d) Scatter plot of the MDsLDR-filtered Z_{hh} and the OBSpol-filtered Z_{hh}. (e) Raw sP_{hh} spectrogram of Ray 51. (f) MDsLDR-filtered sP_{hh} spectrogram. (g) OBSpol-filtered sP_{hh} spectrogram.

the main reason is the presence of residual ground clutter after the MDsLDR filtering, which is illustrated by Ray 51 in Fig. 11(e)–(g), respectively. Note that both techniques cannot resolve the problem when precipitation and clutter overlap. In that case when precipitation the data are discarded by filtering like at 0 ms^{-1} for Ray 51, the radar observables are presently estimated without interpolation procedure in the spectrogram.

C. Other Case Study

To further assess the performance of the OBSpol filter, a case with severe artifacts is considered. The case occurred

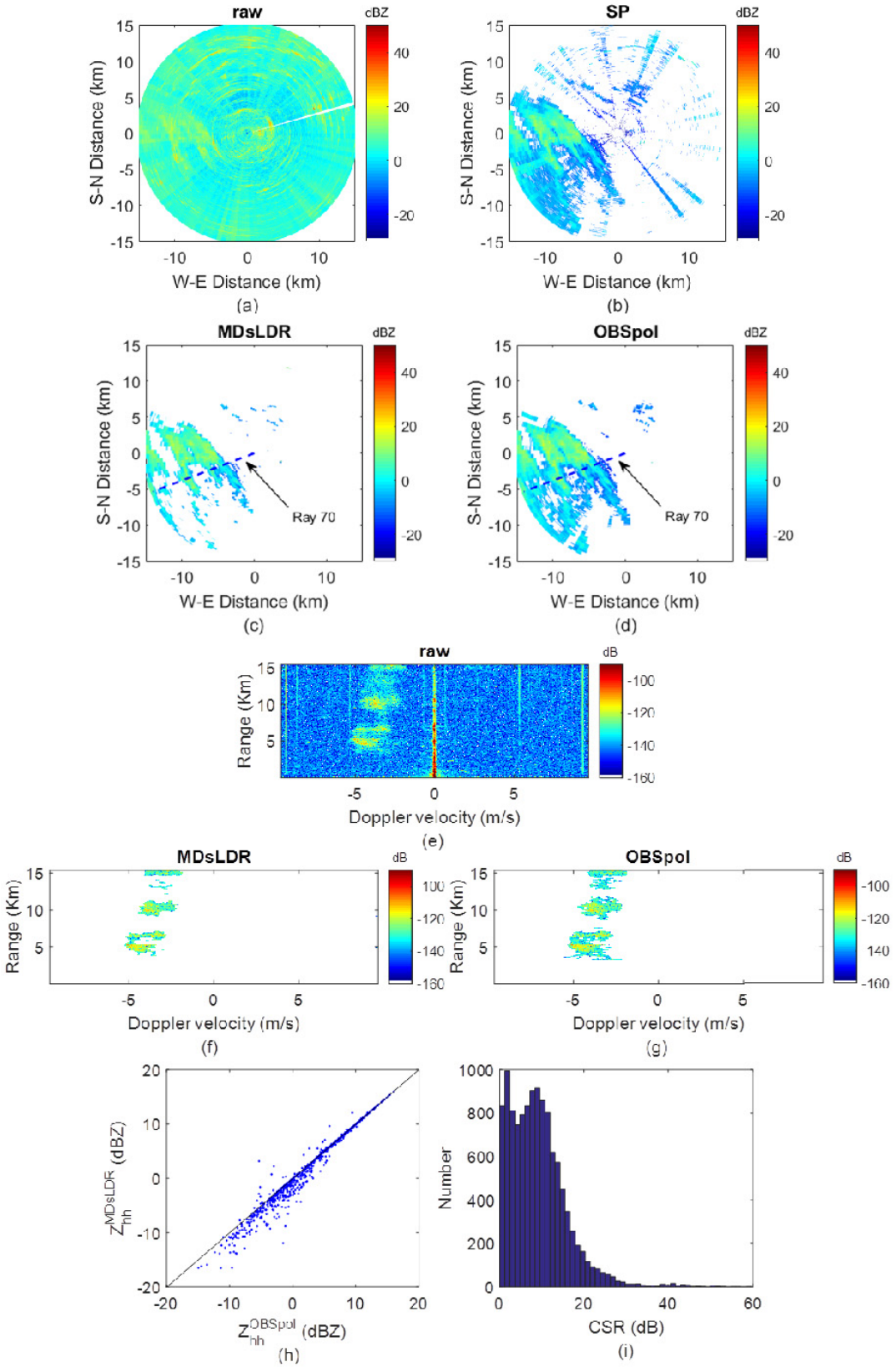

Fig. 12. Performance comparison between MDsLDR and OBSpol filters. Data measured at 12:00 UTC on January 15, 2016. (a) Raw Z_{hh}. (b) Z_{hh} after standard processing. (c) Z_{hh} after MDsLDR filter. (d) Z_{hh} after OBSpol filter. (e) Raw sP_{hh} spectrogram of Ray 70. (f) MDsLDR-filtered sP_{hh} spectrogram. (g) OBSpol-filtered sP_{hh} spectrogram. (h) Scatter plot of MDsLDR-filtered Z_{hh} and OBSpol-filtered Z_{hh}. (i) CSR distribution of the OBSpol filter.

at 12:00 UTC on January 15, 2016. The raw PPI and the one after the standard processing are shown in Fig. 12(a) and (b). It can be observed that the influence of artifacts on radar PPI are severe and artifacts cannot be removed by the standard processing. The PPI of Z_{hh} after the MDsLDR filter and the OBSpol filter are shown in Fig. 12(c) and (d). From this

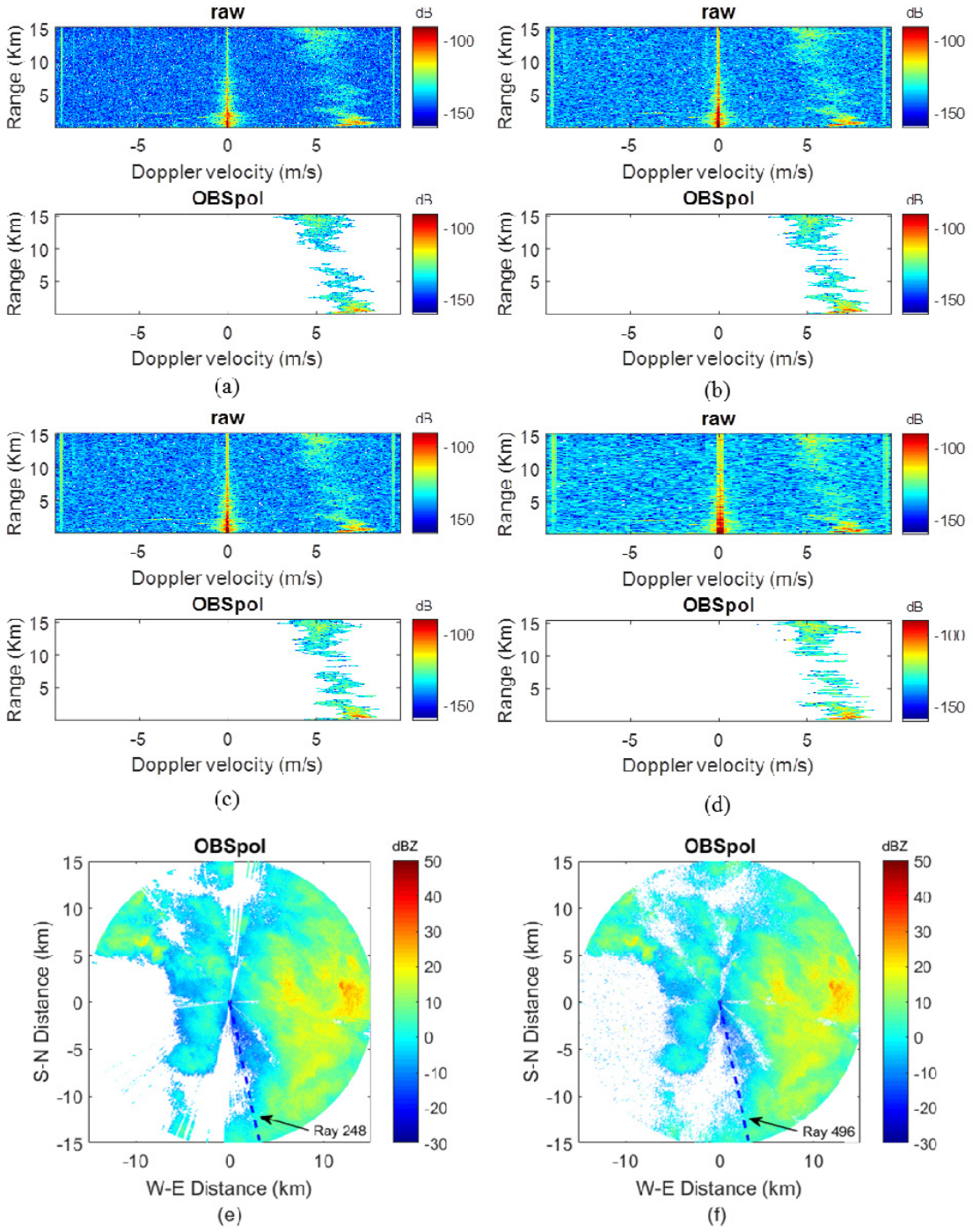

Fig. 13. OBSpol filter applied to radar data with different Doppler velocity resolutions. Data measured at 13:00 UTC on August 22, 2016. (a) sP_{hh} spectrogram with sweep number 512. (b) sP_{hh} spectrogram with sweep number 256. (c) sP_{hh} sectrogram with sweep number 128. (d) sP_{hh} spectrogram with sweep number 64. (e) PPI with sweep number 128. (f) PPI with sweep number 64.

figure, it can be concluded that both the OBSpol filter and the MDsLDR filter can mitigate artifacts while the OBSpol filter can preserve more weak precipitation. Just based on the PPI of Z_{hh}, it is difficult to determine whether the added signal is precipitation or not. Hence, the ray-by-ray inspection has been implemented. Here, Ray 70 is used as an example, and its raw MDsLDR-filtered and OBSpol-filtered spectrograms are presented in Fig. 12(e)–(g), respectively.

From Fig. 12(e), it is obvious that the measurement is severely contaminated by narrowband moving artifacts. Both the MDsLDR and OBSpol filters can remove the nonstationary artifacts, the noise, and the ground clutter, and they can keep the precipitation having moderate SNR. However, less weak precipitation is preserved after the MDsLDR filtering, while the OBSpol filter can keep the weak precipitation locating on the edge of the precipitation area. This is confirmed

TABLE IV
PARAMETER SELECTION FOR DIFFERENT DOPPLER VELOCITY RESOLUTIONS

Sweep number	Doppler velocity resolution (m/s)	averaging size	Ray No	L	T_1	r	T_3
512	3.8×10^{-2}	7	68	5	0.95	3	11
256	7.5×10^{-2}	5	136	4	0.94	3	10
128	1.5×10^{-1}	5	272	3	0.91	2	7
64	3.0×10^{-1}	5	544	1	0.90	2	5

by the scatter plot of the MDsLDR-filtered Z_{hh} and the OBSpol-filtered Z_{hh} in Fig. 12(h). Finally, the histogram of the CSR of the OBSpol filter is shown in Fig. 12(i). Note that the maximum CSR, in this case, is 58.3 dB.

D. Impact of Doppler Velocity Resolution

The operational weather radars tend to have shorter dwell time due to the requirement of faster updating atmospheric changes. This tendency means that the proposed clutter mitigation technique should also work with smaller pulse numbers. This section will further verify the effectiveness of the OBSpol filter regarding different Doppler velocity resolutions.

Since the total sweep number of one IDRA PPI N_{PPI} is fixed, and it meets

$$N_{\text{PPI}} = N_{\text{Ray}} \times N_{\text{Doppler}} \tag{18}$$

where N_{Ray} is total ray number in the PPI and N_{Doppler} is the sweep number chosen for Doppler processing. To get the same data for comparison, the increasing multiple of the ray number is the same as the decreasing multiple of sweep number for Doppler processing in the data selection.

Using the same data measured at 13:00 UTC on August 22, 2014 which is obtained in the operational mode (i.e., pulse repetition frequency around 2.4 kHz), we set the sweep number N_{Doppler} to 512, 256, 128, and 64 for the Doppler processing to explore the OBSpol filter performance. Ray 68, Ray 136, Ray 272, and Ray 544 are considered for the parameter selection which obeys the same principle of Section III-B, as shown in Table IV. Note that the selection of L is obtained by the observation of the spectral width of the narrowband moving clutter. While the decrease of T_1 is due to the smaller sweep number selected for Doppler processing which means the spectral SNR is decreasing, leading to a decrease of the spectral copolar correlation coefficient.

With the parameter selection in Table IV, another ray than the study case Ray 68 is evaluated and the spectrogram results of Ray 62, Ray 124, Ray 248, and Ray 496 related to different Doppler velocity resolutions are shown in Fig. 13(a)–(d), respectively. In addition, the filtered PPIs with sweep number 128 and 64 are shown in Fig. 13(e) and (f). From these results, we can conclude that with the decrease of Doppler velocity resolution, the performance of keeping weak precipitation also degrades. The reason is that the OBSpol filter, taking advantage of range-Doppler continuity of precipitation, will perform better with more data in the range-Doppler spectrogram. However, qualitatively acceptable results in preserving the precipitation and removing narrowband clutter (both moving and stationary) and noise can still be obtained in all the situations. This shows the potential that the OBSpol filter can be used for different Doppler velocity resolutions.

V. CONCLUSION

Aiming at removing both stationary and moving clutter and retaining precipitation for dual-polarization weather radar which does not measure cross-polar backscattering, this paper puts forward a new clutter suppression method named the OBSpol filter. Taking advantage of the spectral polarimetric feature and the range-Doppler continuity of precipitation, the OBSpol filter is implemented in the range-Doppler spectrogram to mitigate the clutter and noise. The filter is divided into four steps. First, the spectral polarimetric observables are utilized to generate one binary mask where "1" indicates the precipitation. In Step 2, the mathematical morphology method is used to recover the missing precipitation areas of the obtained mask. Based on the reconstructed mask in Step 2, the contiguous bins having values "1" are selected and integrated into several separate objects in Step 3. Next, in Step 4, whether the produced objects are precipitation or not will be further decided based on an appropriate observable. Thus, a filtering mask can be obtained by summing up the filtered separated objects, which is implemented on the raw range-Doppler spectrogram to keep the precipitation and remove the clutter and noise.

The OBSpol filter can be very general due to different spectral polarimetric filtering strategies in Step 1 and different observable selection in Step 4, which depend on the type of clutter encountered and based on the clutter feature study. The OBSpol filter is a spectrogram-by-spectrogram clutter mitigation technique which integrates clutter detection and filtering together. In this paper, the OBSpol filter is specifically designed for narrowband clutter (both stationary and moving) mitigation in the polarimetric Doppler radar IDRA. In the situation of IDRA which simulates dual-polarization radar without cross-polar measurements, the spectral copolar correlation coefficient filtering and the notch filter around 0 ms^{-1} are combined in Step 1 and the extra observable in Step 4 is the spectral width. The OBSpol filter can remove the ground clutter, the noise, and the moving artifacts, which are not overlapping with precipitation. In the cases where clutter mixes with precipitation, other techniques should be combined. Compared with one existing method, namely, the MDsLDR filter, both filters can remove narrowband clutter (i.e., ground clutter and moving artifacts) and noise, and they tend to have the same performance in keeping precipitation with a reflectivity larger than 10 dBZ, while OBSpol filter is better in weak precipitation preservation due to the more

advanced signal processing technique adopted in the filter design. Two precipitation cases—1) moderate precipitation with large scale and 2) light precipitation with severe artifact contamination—are used to assess the performance and make the comparison.

There are several advantages of the OBSpol filter. Apart from the good performance in clutter mitigation and precipitation preservation, this technique is easy to implement, and it has relatively low computation complexity. In addition, the spectral polarimetric features can be the observables of dual-polarization weather radar without cross-polar measurements. Last but not least, the OBSpol filter can be used with different Doppler velocity resolutions. Hence, the OBSpol filter can be applied in real-time for dual-polarization operational weather radar. It is foreseeable that the OBSpol filter can be extended to remove different types of weather radar clutter with proper observable selection. However, the OBSpol filter cannot resolve the problem when precipitation is mixed with clutter. It is expected that in absence of moving clutter when precipitation overlaps with ground clutter, the GMAP, or CLEAN-AP will perform better than the OBSpol filter. More research can be done in these directions in the future.

ACKNOWLEDGMENT

The authors would like to thank P. Hoogeboom for his discussion on the topic of radar signal processing. They would also like to thank the anonymous reviewers for their constructive reviews, which helped to improve this paper.

REFERENCES

[1] R. J. Doviak and D. S. Zrnic, *Doppler Radar & Weather Observations*. New York, NY, USA: Academic, 2014.

[2] R. J. Doviak, V. Bringi, A. Ryzhkov, A. Zahrai, and D. Zrnić, "Considerations for polarimetric upgrades to operational WSR-88D radars," *J. Atmos. Ocean. Technol.*, vol. 17, no. 3, pp. 257–278, 2000.

[3] H. Chen and V. Chandrasekar, "The quantitative precipitation estimation system for Dallas–Fort Worth (DFW) urban remote sensing network," *J. Hydrol.*, vol. 531, pp. 259–271, Dec. 2015.

[4] H. Chen, V. Chandrasekar, and R. Bechini, "An improved dual-polarization radar rainfall algorithm (DROPS2.0): Application in NASA IFloodS field campaign," *J. Hydrometeorol.*, vol. 18, no. 4, pp. 917–937, 2017.

[5] D. Rezacova, Z. Sokol, and P. Pesice, "A radar-based verification of precipitation forecast for local convective storms," *Atmos. Res.*, vol. 83, no. 2, pp. 211–224, 2007.

[6] H. T. L. Huong and A. Pathirana, "Urbanization and climate change impacts on future urban flooding in Can Tho city, Vietnam," *Hydrol. Earth Syst. Sci.*, vol. 17, no. 1, pp. 379–394, 2013.

[7] A. Hamidi, N. Devineni, J. F. Booth, A. Hosten, R. R. Ferraro, and R. Khanbilvardi, "Classifying urban rainfall extremes using weather radar data: An application to the greater New York area," *J. Hydrometeorol.*, vol. 18, no. 3, pp. 611–623, 2017.

[8] T. F. Stocker *et al.*, "Climate change 2013: The physical science basis," in *Intergovernmental Panel on Climate Change, Working Group I Contribution to the IPCC Fifth Assessment Report (AR5)*. New York, NY, USA: Cambridge Univ Press, 2013.

[9] A. Siggia and R. Passarelli, "Gaussian model adaptive processing (GMAP) for improved ground clutter cancellation and moment calculation," in *Proc. Eur. Radar Meteorol. Hydrol.*, vol. 2, 2004, pp. 421–424.

[10] D. A. Warde and S. M. Torres, "The autocorrelation spectral density for Doppler-weather-radar signal analysis," *IEEE Trans. Geosci. Remote Sens.*, vol. 52, no. 1, pp. 508–518, Jan. 2014.

[11] S. Torres, D. Warde, and D. Zrnic, "Signal design and processing techniques for WSR-88D ambiguity resolution: Part 15 the CLEAN-AP filter," Nat. Severe Storms Lab., Norman, OK, USA, Tech. Rep., 2012.

[12] P. M. Stepanian and K. G. Horton, "Extracting migrant flight orientation profiles using polarimetric radar," *IEEE Trans. Geosci. Remote Sens.*, vol. 53, no. 12, pp. 6518–6528, Dec. 2015.

[13] D. S. Zrnić and A. V. Ryzhkov, "Observations of insects and birds with a polarimetric radar," *IEEE Trans. Geosci. Remote Sens.*, vol. 36, no. 2, pp. 661–668, Mar. 1998.

[14] V. Melnikov, M. Leskinen, and J. Koistinen, "Doppler velocities at orthogonal polarizations in radar echoes from insects and birds," *IEEE Geosci. Remote Sens. Lett.*, vol. 11, no. 3, pp. 592–596, Mar. 2014.

[15] V. M. Melnikov, M. J. Istok, and J. K. Westbrook, "Asymmetric radar echo patterns from insects," *J. Atmos. Ocean. Technol.*, vol. 32, no. 4, pp. 659–674, 2015.

[16] L. Alku, D. Moisseev, T. Aittomäki, and V. Chandrasekar, "Identification and suppression of nonmeteorological echoes using spectral polarimetric processing," *IEEE Trans. Geosci. Remote Sens.*, vol. 53, no. 7, pp. 3628–3638, Jul. 2015.

[17] J. Yin, O. Krasnov, C. Unal, S. Medagli, and H. Russchenberg, "Spectral polarimetric features analysis of wind turbine clutter in weather radar," in *Proc. 11th Eur. Conf. Antennas Propag. (EUCAP)*, 2017, pp. 3351–3355.

[18] B. M. Isom *et al.*, "Detailed observations of wind turbine clutter with scanning weather radars," *J. Atmos. Ocean. Technol.*, vol. 26, no. 5, pp. 894–910, 2009.

[19] F. Kong, Y. Zhang, and R. Palmer, "Wind turbine clutter mitigation for weather radar by adaptive spectrum processing," in *Proc. IEEE Radar Conf.*, May 2012, pp. 0471–0474.

[20] F. Nai, S. Torres, and R. Palmer, "On the mitigation of wind turbine clutter for weather radars using range-Doppler spectral processing," *IET Radar, Sonar Navigat.*, vol. 7, no. 2, pp. 178–190, 2013.

[21] F. Uysal, I. Selesnick, and B. M. Isom, "Mitigation of wind turbine clutter for weather radar by signal separation," *IEEE Trans. Geosci. Remote Sens.*, vol. 54, no. 5, pp. 2925–2934, May 2016.

[22] R. Nepal, J. Cai, and Z. Yan, "Micro-Doppler radar signature identification within wind turbine clutter based on short-CPI airborne radar observations," *IET Radar, Sonar Navigat.*, vol. 9, no. 9, pp. 1268–1275, Dec. 2015.

[23] E. Saltikoff *et al.*, "The threat to weather radars by wireless technology," *Bull. Amer. Meteorol. Soc.*, vol. 97, no. 7, pp. 1159–1167, 2016.

[24] J. Yin, C. M. H. Unal, and H. W. J. Russchenberg, "Narrow-band clutter mitigation in spectral polarimetric weather radar," *IEEE Trans. Geosci. Remote Sens.*, vol. 55, no. 8, pp. 4655–4667, Aug. 2017.

[25] J. Yin, C. Unal, M. Schleiss, and H. Russchenberg, "Radar target and moving clutter separation based on the low-rank matrix optimization," *IEEE Trans. Geosci. Remote Sens.*, vol. 56, no. 8, pp. 4765–4780, Aug. 2018.

[26] O. A. Krasnov and A. G. Yarovoy, "Polarimetric micro-Doppler characterization of wind turbines," in *Proc. 10th Eur. Conf. Antennas Propag. (EuCAP)*, 2016, pp. 1–5.

[27] (Jun. 2018). *X-Band Radar of Bonn University*. [Online]. Available: https://www.meteo.uni-bonn.de/messdaten/radarbilder/aktuelle-bilder-1/bonn/ppi

[28] C. S. Morse, R. K. Goodrich, and L. B. Cornman, "The NIMA method for improved moment estimation from Doppler spectra," *J. Atmos. Ocean. Technol.*, vol. 19, pp. 274–295, Mar. 2002.

[29] S. Bachmann and D. Zrnić, "Spectral density of polarimetric variables separating biological scatterers in the VAD display," *J. Atmos. Ocean. Technol.*, vol. 24, no. 7, pp. 1186–1198, 2007.

[30] C. Unal, "Spectral polarimetric radar clutter suppression to enhance atmospheric echoes," *J. Atmos. Ocean. Technol.*, vol. 26, no. 9, pp. 1781–1797, 2009.

[31] T. D. Crum and R. L. Alberty, "The WSR-88D and the WSR-88D operational support facility," *Bull. Amer. Meteorol. Soc.*, vol. 74, pp. 1669–1687, Sep. 1993.

[32] (Jun. 2018). *NWS WSR-88D Level II Data*. [Online]. Available: https://www.roc.noaa.gov/wsr88d/Level_II/Level2Info.aspx

[33] D. N. Moisseev and V. Chandrasekar, "Polarimetric spectral filter for adaptive clutter and noise suppression," *J. Atmos. Ocean. Technol.*, vol. 26, no. 2, pp. 215–228, 2009.

[34] I. R. Ivić, C. Curtis, and S. M. Torres, "Radial-based noise power estimation for weather radars," *J. Atmos. Ocean. Technol.*, vol. 30, no. 12, pp. 2737–2753, 2013.

[35] P. Soille, *Morphological Image Analysis: Principles and Applications*. Springer, 2013.

[36] R. Fisher, S. Perkins, A. Walker, and E. Wolfart. (Jun. 2018). *Connected Components Labeling*. [Online]. Available: http://homepages.inf.ed.ac.uk/rbf/HIPR2/label.htm

[37] (Jun. 2018). *Flood Fill*. [Online]. Available: https://en.wikipedia.org/wiki/Flood_fill
[38] U. C. Benz, P. Hofmann, G. Willhauck, I. Lingenfelder, and M. Heynen, "Multi-resolution, object-oriented fuzzy analysis of remote sensing data for GIS-ready information," *ISPRS J. Photogramm. Remote Sens.*, vol. 58, nos. 3–4, pp. 239–258, Jan. 2004.
[39] J. Figueras i Ventura, "Design of a high resolution X-band Doppler polarimetric radar," Ph.D. dissertation, Dept. Telecommun., Delft Univ. Technol., Delft, The Netherlands, 2009.
[40] (Jun. 2018). *Near-Realtime Reflectivity Measurements of IDRA*. [Online]. Available: http://ftp.tudelft.nl/TUDelft/irctr-rse/idra
[41] (Jun. 2018). *IDRA Data*. [Online]. Available: https://data.4tu.nl/repository/collection:cabauw
[42] C. M. H. Unal and D. N. Moisseev, "Combined Doppler and polarimetric radar measurements: Correction for spectrum aliasing and nonsimultaneous polarimetric measurements," *J. Atmos. Ocean. Technol.*, vol. 21, no. 3, pp. 443–456, 2004.

Jiapeng Yin (S'16) received the B.S. degree in information engineering from the National University of Defense Technology, Changsha, China, in 2012. He is currently pursuing the Ph.D. degree with the Department of Geoscience and Remote Sensing, Delft University of Technology, Delft, The Netherlands.

His research interests include weather radar clutter suppression and weather radar calibration.

Christine Unal received the master's degree in physics from the University of Nice Sophia Antipolis, Nice, France, in 1986, and the D.E.A. degree in physics for remote sensing from the University of Paris, Paris, France, in 1987.

In 1988, she joined the Delft University of Technology, Delft, The Netherlands. She was with the International Research Center for Telecommunications and Radar, Delft University of Technology, where she has been with the Department of Geoscience and Remote Sensing and the Climate Institute, since 2012. She was involved in radar polarimetric calibration and radar spectral polarimetry (quasi-simultaneous Doppler spectra of polarimetric measurements, their processing, and their interpretation). Since 2003, she has been involved in the processing of atmospheric echoes. She is currently a Research Scientist with Delft University of Technology. Her research interests include weather/atmospheric radar signal processing and searching for new retrieval techniques to estimate microphysical and dynamical properties of precipitation using ground-based radars.

Herman Russchenberg was involved in theoretical as well as experimental research of the scattering process and the retrieval of geophysical parameters from radar and lidar measurements. He is currently the Director of the Climate Institute and the Head of the Department of Geoscience and Remote Sensing, Delft University of Technology. He is involved in remote sensing of clouds and precipitation with ground-based radar, lidar, and microwave radiometry. He is one of the leading scientists of the Cabauw Experimental Site for Atmospheric Research, The Netherlands.